Spacing and strength of active continental strike-slip faults

Andrew V. Zuza, An Yin, Jessica Lin, and Ming Sun

Supplementary Material

- Figure A1. Physical and mechanical properties of experimental materials.
- The stress-shadow model applied to the analogue experiments
- Figure A2. Coordinate system and schematic diagrams showing the validation of the stress-shadow model by analogue experiments
- Figure A3. Earthquake depth plotted as a function of horizontal distance for California and Asia.
- Supplementary references

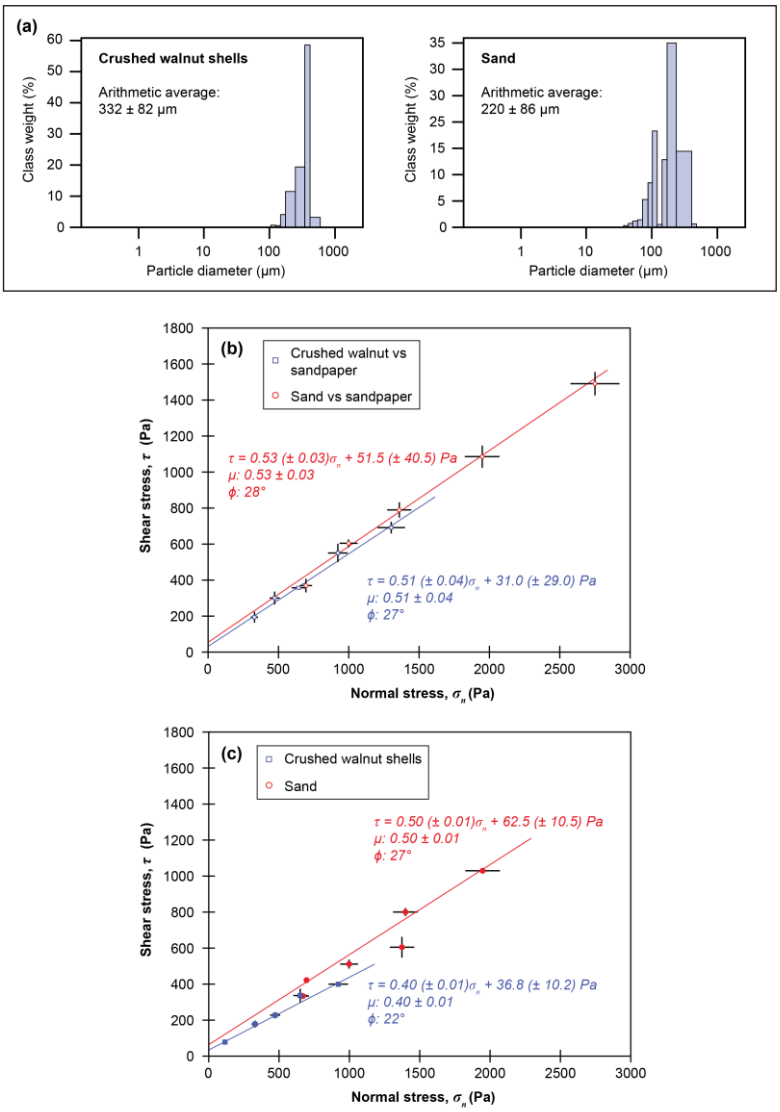

Figure A1. Physical and mechanical properties of experimental materials. (a) Grain size distributions for dry crushed walnut shells and dry sand using the methods of Blott and Pye (2001). (b) Measured relationships between shear stress and normal stress for both dry crushed walnut shells and dry sand again P100 sandpaper. (c) Measured relationship between shear stress and normal stress for dry crushed walnut shells and dry sand. For both (b) and (c), the best-fit linear regression for each material yields the cohesive strength, coefficient of internal friction, and angle of internal friction, which are reported in Table 1 of the main text. Previous studies report an angle of friction (ϕ) of 30.3–32.8º and a cohesive strength (C_0) of 80 ± 22 Pa for dry sand (Maillot and Koyi, 2006) and ϕ and C_0 of 38.5-40.8º and 23-13 Pa for crushed walnut shells (Cruz et al., 2008). The procedure of the Hubbert-type experiments in (b) and (c) are described in greater detail by Hubbert (1951), Schellart (2000), Maillot and Koyi (2006), and Cruz et al. (2008).

The stress-shadow model applied to the analogue experiments

We first determine the shear stress on a vertical plane parallel to the movement direction of the sliding plate (Fig. A2). The stress equilibrium equation in the sliding plate direction *x* can be written as

$$\frac{\partial \sigma_{xx}}{\partial x} + \frac{\partial \sigma_{xy}}{\partial y} + \frac{\partial \sigma_{zx}}{\partial z} = 0 \quad \text{(S1)}$$

where σ_{xx} is the normal stress on vertical planes perpendicular to the sliding plate, σ_{xy} is the shear stress on vertical planes parallel to the movement direction of the sliding plate, and σ_{zx} is the shear stress on planes parallel to the sliding plate and in the direction of the sliding plate motion (Fig. A2a). Assuming that σ_{xx} is in a state of lithostatic stress, we have $\sigma_{xx} = -\rho g z$ (we use the sign convention that compressive stress is negative). Based on the symmetry of the problem, $\sigma_{xy}(y = 0) = 0$ (i.e., on the vertical plane along the middle dividing line of the sliding plate) because on the vertical plane of $y = 0$ the shear sense switches. Finally, our measurements of the frictional properties between sand/crushed walnut shells against the underlying sand paper require that $\sigma_{zx} = -\mu_b \rho g z - C_b$, and $\sigma_{zx}(z = h) = -\mu_b \rho g h - C_b$, where μ_b is the friction coefficient of sand/crushed walnut shells against the sand paper, and C_b is the corresponding cohesive strength of the dry sand/crushed walnut shells. The negative signs in the expression of $\sigma_{zx} = -\mu_b \rho g z - C_b$ are the results of our assigned sign convention.

Under the aforementioned conditions, we can solve equation (S1) and obtain the "sidewall" shear stress on a plane perpendicular to the sliding plate and parallel to the movement direction of the sliding plate (Fig. A2a). Specifically,

$$\frac{\partial \sigma_{xx}}{\partial x} = 0 \quad \text{(S2)}$$

$$\frac{\partial \sigma_{zx}}{\partial z} = -\mu_b \rho g \quad \text{(S3)}$$

Inserting (S2) and (S3) into equation (S1), we have

$$\frac{\partial \sigma_{xy}}{\partial y} = -\mu_b \rho g \quad \text{(S4)}$$

Equation (S4) yields

$$\sigma_{xy} = -\mu_b \rho g y + f(x, z) + a_0 \quad \text{(S5)}$$

where $f(x, z)$ is an arbitrary function of *x* and *z* when solving σ_{xy} and a_0 is a constant. The boundary condition of $\sigma_{xy}(y = 0) = 0$ requires that $f(x, z) + a_0 = 0$, which leads to a simplified equation (S5) as

$$\sigma_{xy} = \sigma_{sidewall} = \mu_b \rho g y \quad \text{(S6)}$$

The above equation, which is given as equation (16) in the main text, indicates that the sidewall shear stress depends on the coefficient of basal friction, the density of the experimental material, and the surface gravity. Equation (S6) also shows that the sidewall shear stress increases with its

distance from the central dividing line of the sliding plate, where $y = 0$ (Fig. A2). Our interest is to determine the magnitude of the shear stress parallel to the Riedel shears, which trend at an angle of θ from $\sigma_{sidewall}$ (Fig. A2b). A transformation of coordinates allows us to determine the "fault parallel" stress, σ_{fp}. The shear stress applied on planes parallel to the Riedel shear fractures can be expressed as

$$\sigma_{fp}^{sand} = \sigma_{sidewall}^{sand} \times \cos 2\theta \tag{S7}$$

and

$$\sigma_{fp}^{walnut} = \sigma_{sidewall}^{walnut} \times \cos 2\theta \tag{S8}$$

where $\theta \approx 16°$ as observed in our experiments (i.e., the angle between the sliding direction and the trend of the Riedel shear fractures) (Fig. A2b). Although $\sigma_{xy} = \sigma_{sidewall} = \mu_b \rho g y$ goes to infinite as $y \to \infty$ (Fig. A2c), its induced shear stress σ_{fp} parallel to the Riedel shear stress is finite. This finite value can evaluated at $y = d$, which marks the edge of the shear zone (Fig. A2):

$$\sigma_{fp}^{sand/walnut} = \sigma_{sidewall}^{sand/walnut}(y = d) \times \cos(2\theta) = \mu_b \rho g d \cos(2\theta) \tag{S9}$$

where $\sigma_{fp}(y = d)$ is greater than the yield strength of the experimental material, creating a shear zone in which Riedel shear fractures are created (Figs. A2c and A2d). Shear stress is expected to increase with *y* to some maximum value at the dislocation at the edge of the basal sliding plate (i.e., *y* = *W*). However, once *y* = *d*, we assume that σ_{fp} remains relatively constant at some magnitude slightly greater than Y because the formation of shear fractures within the Riedel shear zone will keep the σ_{fp} from rising further (Fig. A2c). In the above interpretation, σ_{fp} is equivalent to the regional stress ${\sigma_s}^r = \sigma^{bc}$ used in equation (1b).

As the dry sand/crushed walnut shells are both Coulomb materials, their shear strengths increase with normal stress and thus depth. That is, at the surface, the shear strengths of the dry sand/crushed walnut shells are the lowest and equal to the cohesive strength of the experimental materials (Table 1). On the other hand, the shear stress generated by the basal shearing that is parallel to the Riedel shear fractures is vertically uniform, as expressed by $\sigma_{fp} = \mu_b \rho g d \cos(2\theta)$, which is independent of *z*. Under such a stress state, Riedel shear fractures will break first at the surfaces, where the yield strengths of the experimental Coulomb materials are weakest and equal to the cohesive strengths. In this scenario, our stress shadow model from equation (6) of the main text, relating fault spacing *S* to brittle layer thickness *h*, may be written as

$$S = \frac{\bar{Y} - \overline{\sigma^f}}{\sigma^{bc} - \bar{Y}} h = \frac{C_Y - C_f}{\sigma_{fp} - C_Y} h \tag{S10}$$

where $\sigma_{fp} = \mu_b \rho g d \cos(2\theta)$ is the fault-parallel regional shear stress, C_Y is the cohesive strength of the experimental material (same as C_0 in equation (8) in the main text), and C_f is the cohesive strength of the Riedel shear fractures (equal to C_1 in equation (7) of the main text). The

interpretation that the spacing of the observed Riedel shear spacing is controlled by the cohesive strength only, as expressed in equation (S10), explains why the *S/h* ratio is constant in our experiments regardless of changes in the thickness of the experimental materials (i.e., *h*). This would not be the case if a frictional term depending on *h* is involved in equation (S10).

The values of C_Y for dry sand and crushed walnut shells were measured in our study (Table 1), whereas the values of C_f are unknown for both experimental materials. However, from equation (S10), we can estimate C_f if the *S/h* ratio defined in equation (S10) is known.

Based on our experiments with only granular materials, the *S/h* ratio is ~0.68 for dry sand and ~0.82 for crushed walnut shells, respectively (Fig. 4d). In the sand and viscous putty experiments, the *S*/*h* ratio is 0.45-0.56 (average 0.51). Visual observations indicate that $d \approx W/3 \approx 2$ cm, which defines the position of the inner boundary of the shear zone, where fault-parallel shear stress (σ_{fp}) exceeds the yield strength of the experimental materials leading to the formation of the Riedel shear fractures. In our experiments, the shear zone boundary location $y = d$ can be determined by the bending segments of the originally straight reference lines that were perpendicular to the movement direction of the sliding plate (e.g., Fig. 4c). This estimate is likely a maximum value.

Using d = 2 cm, μ_b = 0.53 (Table 1), a sand density of 1670 kg/m^3, $\theta = 16°$, and $g = 9.8$ m/s^2, we obtain

$$\sigma_{fp} = \mu_b \rho g d \cos(2\theta) = 147 \text{ Pa} \quad \text{(S11)}$$

Rearranging equation (S10) and inserting known C_Y = 62.5 Pa (Table 1), σ_{fp} = 147 Pa from (S11), and S/h = 0.68 from Fig. 4d, we estimate the cohesive strength of the Riedel shear fractures formed in our dry sand experiments as:

$$C_f^{sand} = C_Y - \frac{S}{h}\left(\sigma_{fp} - C_Y\right) = 5 \text{ Pa} \quad \text{(S12)}$$

For the sand-putty experiments μ_b is ~0.73 (Table 1) and *d* is expected to be smaller because of the effects of distributed basal shear. Using *S*/*h* = 0.52, μ_b = 0.73, d = 1.5 cm, a sand density of 1670 kg/m^3, $\theta = 16°$, and $g = 9.8$ m/s^2, and C_Y = 62.5 Pa, we estimate $C_f^{sand\_putty}$ = 15 Pa.

For crushed walnut shell experiments, we use μ_b = 0.51 (Table 1), a density of 800 kg/m^3, θ = 16º, and g = 9.8 m/s^2 to calculate the fault parallel shear stress as

$$\sigma_{fp} = \mu_b \rho g d \cos(2\theta) = 68 \text{ Pa} \quad \text{(S13)}$$

Using a S/h ratio of 0.82 (Fig. 4d) and a cohesive strength of 36.8 Pa (Table 1), we obtain the corresponding cohesive strength of the Riedel shears that formed in the crushed walnut shells under basal shearing as

$$C_f^{walnut} = C_Y - \frac{S}{h}\left(\sigma_{fp} - C_Y\right) = 11 \text{ Pa} \quad \text{(S14)}$$

We find that the estimated cohesive strengths of the newly created fractures in both dry sand and crushed walnut shells are reasonable: (1) they are all positive values, and (2) they are smaller

than the cohesive strength of materials in which the shear fractures formed. The above consistency provides validation of our proposed stress-shadow model.

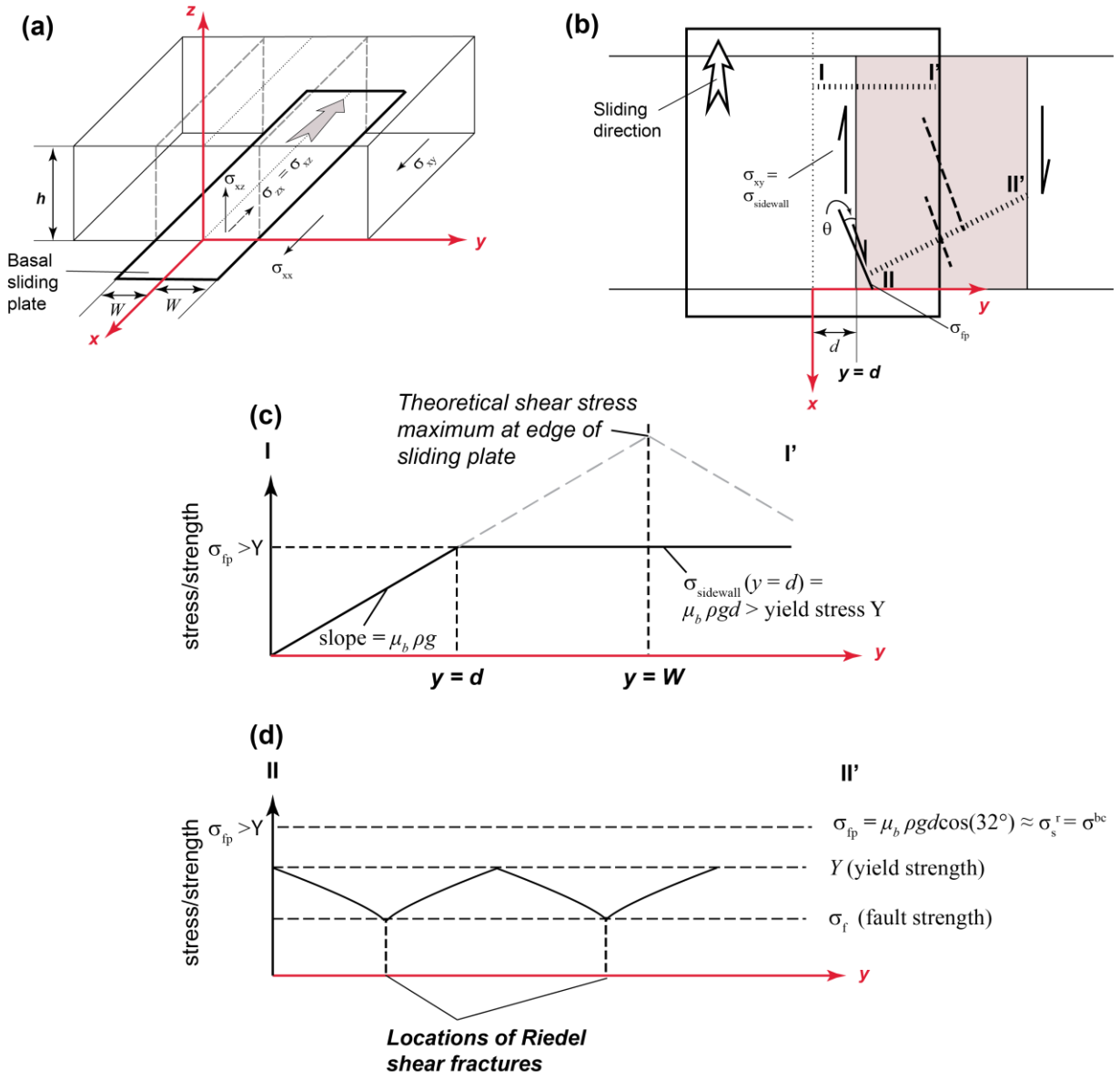

Figure A2. (a) Coordinate system of reference. The box represents the region occupied by the experimental materials (i.e., dry sand and crushed walnut shells). *h*, thickness of the experimental material; *W*, the half width of the basal sliding plate; *x*-*y* plane lies at the base of the experimental set up and $y = 0$ represents the central dividing line of the sliding plate. (b) Plan view of the sidewall shear stress on a vertical plane at the edge of the shear zone that is parallel to the sliding plate direction and perpendicular to the basal plane. Also shown is the angular relationship between the sidewall shear stress and the fault-parallel shear stress. The location of the inner boundary of the shear zone is marked by $y = d$ and the edge of the basal-sliding plate is $y = w$. Note that although the maximum shear stress should occur at $y = w$, we assume that the shear stress must remain at or below the shear fracture strength of the materials. Lines I-I' and II-II' are cross sections along which the stress distributions are shown in (c) and (d). (c) Postulated magnitude distribution of the sidewall shear stress across the shear zone. (d) Postulated magnitude distribution of the fault-parallel shear stress across the Riedel shear fractures in the shear zone.

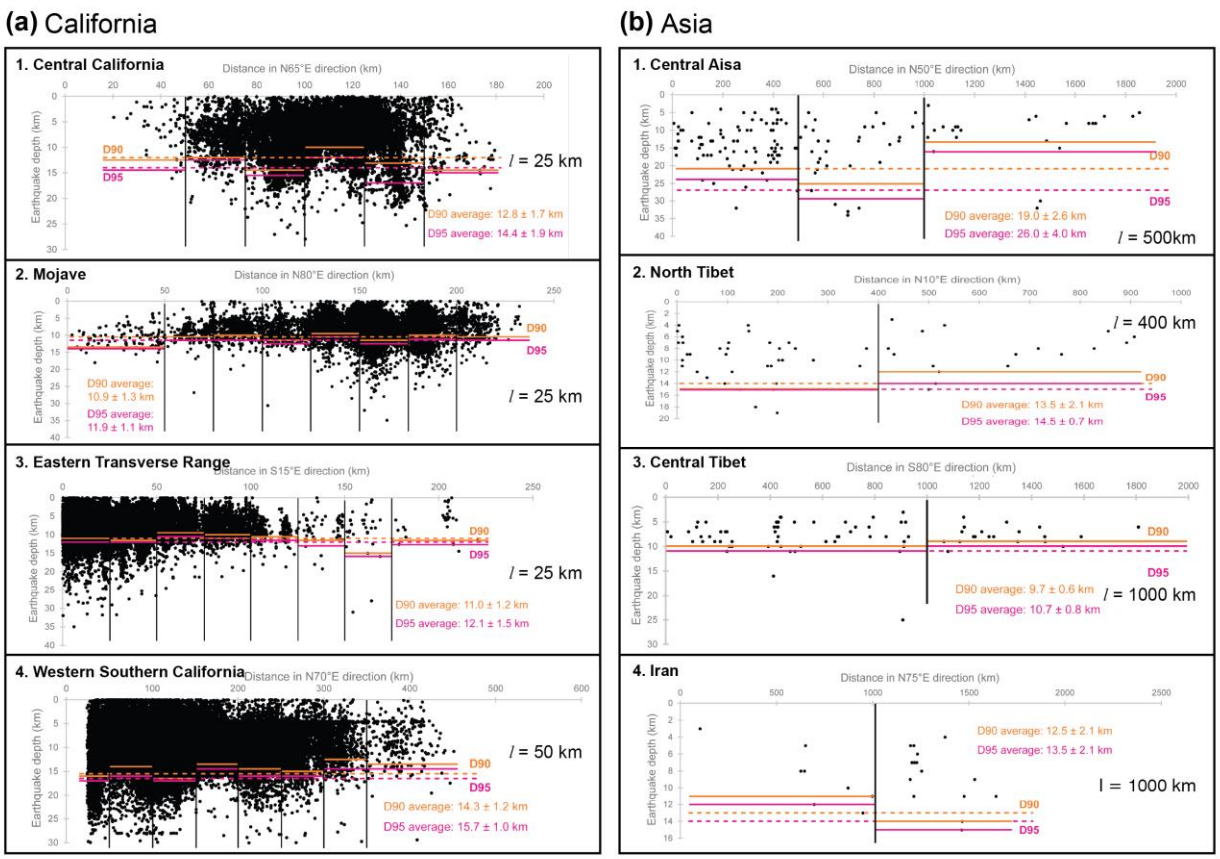

Figure A3. Earthquake depth plotted as a function of horizontal distance along a profile line perpendicular to the fault strike of each domain from (a) California and (b) Asia. For this plot, the cutoff depth above which 95% (D95) and 90% (D90) seismicity is contained in the crust was calculated (e.g., Sibson, 1982) (Table 2 of main text). Dashed lines represent the bulk averaged D90 (orange) and D95 (pink) depths without dividing each profile into segments. In contrast, the solid lines represent the D90 (orange) and D95 (pink) depths in each segment with a segment length *l*.

Supplementary references:

Blott, S. J., and Pye, K., 2001, GRADISTAT: a grain size distribution and statistics package for the analysis of unconsolidated sediments: Earth surface processes and Landforms, v. 26, no. 11, p. 1237-1248.

Cruz, L., Teyssier, C., Perg, L., Take, A., and Fayon, A., 2008, Deformation, exhumation, and topography of experimental doubly-vergent orogenic wedges subjected to asymmetric erosion: Journal of Structural Geology, v. 30, no. 1, p. 98-115.

Hubbert, M. K., 1951, Mechanical basis for certain familiar geologic structures: Geological Society of America Bulletin, v. 62, no. 4, p. 355-372.

Jaeger, J. C., Cook, N. G., and Zimmerman, R., 2009, Fundamentals of rock mechanics: John Wiley & Sons.

Maillot, B., and Koyi, H., 2006,. Thrust dip and thrust refraction in fault-bend folds: analogue models and theoretical predictions: Journal of Structural Geology, v. 28, no. 1, p. 36-49.

Schellart, W. P., 2000, Shear test results for cohesion and friction coefficients for different granular materials: scaling implications for their usage in analogue modelling: Tectonophysics, v. 324, no. 1, p. 1-16.

Sibson, R. H., 1982, Fault zone models, heat flow, and the depth distribution of earthquakes in the continental crust of the United States: Bulletin of the Seismological Society of America, v. 72, no. 1, p. 151-163.